In situ photoelectrochemical activation of sulfite by MoS$_2$ photoanode for enhanced removal of ammonium nitrogen from wastewater

Xiang Fan, Yurou Zhou, Guan Zhang*, Tongzhou Liu, Wenyi Dong

School of Civil and Environmental Engineering, Harbin Institute of Technology, Shenzhen (HITSZ), Shenzhen 518055, PR China

ABSTRACT

The advanced oxidation processes (AOPs) based on oxysulfur radicals (SO$_3$$^{\cdot-}$, SO$_4$$^{\cdot-}$ and SO$_5$$^{\cdot-}$) has been receiving growing attention in wastewater treatment. In this study, we report the in situ photoelectrochemical activation of sulfite to produce oxysulfur radicals with MoS$_2$ nanosheets as a wide spectrum absorptive photo-anode. At alkaline condition, the selective and efficient conversion of ammonia to dinitrogen was exclusively achieved in the presence of sulfite electrolyte under visible light irradiation. The sulfite plays multiple roles such as working as hole scavenger for improving stability of MoS$_2$ electrode by inhibiting photo-corrosion and serving as precursor of oxysulfur radicals in the meantime. The influences of radical scavenger, dissolved oxygen and electrolyte on the photoelectrochemical, electrochemical and photochemical conversion of ammonia verified that oxysulfur radicals are more powerful than hydroxyl radicals in terms of ammonia conversion. The proposed system appears to be applicable to in situ treatment of wastewater containing of ammonia and sulfite pollutants, such as wastewater from ammonia-absorption-desulfurization of combustion smoke. This work also provides a new protocol in the design of new AOPs, where oxysulfur radicals can work together with hydroxyl radicals for simultaneous pollutants degradation and detoxification.

1. Introduction

The ammonium nitrogen (NH$_3$–N) species in wastewater poses a great threat to the environment and subsequently to human health. Therefore, a variety of traditional techniques such as biological treatment, membrane separation, ion exchange, chemical oxidation, physical adsorption and breakpoint chlorination [1–3], and new remediation techniques such as electrochemical oxidation and stripping [4,5], have been studied for the removal of NH$_3$–N from wastewater. However, effective, low-cost and environmental-friendly approach for removal of NH$_3$–N from wastewater has yet to be found. As one of the advanced oxidation processes (AOPs) for potential environmental remediation, photochemical or photoelectrochemical (PEC) degradation of different types of water pollutants has been intensively studied, mainly because of their advantages such as utilization of solar energy as driving force and without input of additional chemicals by in situ generation of active oxidation species (radical species, valence band hole, etc.). For example, photocatalytic removal of ammonium nitrogen has been attempted recently [6–15]. In these work, both ·OH radicals and valence band holes generated from photoirradiation of semiconductor photocatalysts are assumed as the main oxidants. However, the ·OH radicals based AOPs may not suitable for removal of ammonia

species regardless of their strong oxidation power (2.80 V vs. SHE). From structural point of view, ·OH with strong electrophilic character has similar electronic structure with NH$_3$ and H$_2$O molecules, thus NH$_3$ in H$_2$O can not be easily and selectively attacked by ·OH radicals. Normally, larger organic pollutant molecules (dyes, pesticides, aromatic phenols etc.) bearing with electron-withdrawing functional groups are often targeted as model substrates for evaluating oxidation performance of ·OH radicals. Furthermore, complete removal of ammonia nitrogen from water cannot be achieved, since most of ammonia species are converted into nitrite and nitrate ions by the ·OH radicals mediated oxidation [6–15].

With a rapid development of AOPs, other radical species including carbonate, sulfate, phosphate, chloride and sulfite radicals draw much attention because they can also be utilized as oxidants and extend the applications of AOPs for environmental remediation [16–20]. For example, in situ photochemical activation of sulfate to generate SO$_4$$^{\cdot-}$ with bismuth phosphate photocatalyst for enhanced degradation of 2,4-dichlorophenol in water has been reported [16]. Cl· and Cl$_2$$^{\cdot-}$ have been demonstrated to be more efficient than ·OH in terms of converting ammonia species in electrochemical or photoelectrochemical systems. Hoffman's group specifically investigated electrochemical removal of ammonia in latrine wastewater via in situ generated chlorine species

---

utilizing chloride anion in wastewater [17–19]. Recently, Zhou's group reported a novel solar-driven photoelectrocatalytic-chlorine radical reactions system based on WO_3 electrode for highly selective transformation of ammonia nitrogen to N_2 [20]. Compared to photochemical removal of pollutants operated in slurry system, PEC system enables easy recovery of photocatalyst and facilitates photo-generated charge separation, which has more application potential in real wastewater treatment [21,22]. In order to apply the PEC remediation technique practically, some key issues are needed to be solved, especially the development of low-cost and stable electrode materials that can efficiently utilize solar light irradiation is crucial and thus intense research has been focused on this topic [23,24].

MoS_2, emerging as a flagship two-dimensional material, has semiconducting behavior with an indirect-direct band gap transition between bulk (ca 1.1–1.3 eV) and monolayer (ca 1.7–1.9 eV) form. Both theoretical calculation and experimental studies suggest that the monolayer and few-layer MoS_2 have suitable band edge positions for water splitting [25]. Therefore, large number of research papers relevant to MoS_2 focus on solar energy conversion related applications, such as solar cells [26], photocatalysis [27], and PEC water splitting [28]. A variety of nanostructured MoS_2 materials (eg. nanoflakes, nanoflowers, quantum dots and nanosheets) have been developed as visible light sensitizers of other semiconductors in both photocatalytic and photoelectrochemical systems [29–31]. Although nanostructured MoS_2 has been frequently investigated as visible light sensitizer of other semiconductors, the intrinsic photochemical or PEC properties of MoS_2 itself have been much less investigated. Particularly, the PEC degradation of pollutants utilizing MoS_2 photoanode has been rarely studied and thus it is necessary to explore the PEC degradation behavior of nanostructured MoS_2.

Herein, we report our work with trying to realize in situ PEC activation of sulfite in water, in order to generate oxysulfur ($SO_3{}^{\cdot -}$, $SO_4{}^{\cdot -}$ and $SO_5{}^{\cdot -}$) radicals for efficient removal of ammonia nitrogen by employing few-layered MoS_2 photoanode under visible light irradiation. Firstly, the physicochemical properties of chemically exfoliated MoS_2 nanosheets and the microstructure of MoS_2 photoanode was specifically investigated to optimize photocurrents generation by the MoS_2 photoanode under visible light irradiation. Then, visible light driven PEC activation of sulfite for removal of NH_3 by the optimized MoS_2 photoanode was evaluated, and the effects of different operation parameters (e.g., pH, anodic potential and oxygen concentration), degradation products and mechanism were specifically investigated. The results show that the conversion of NH_3 into N_2 can be markedly improved by the proposed PEC system. We hope that the proposed PEC system could be further developed as an economical, sustainable, and efficient means of ammonia nitrogen polluted wastewater treatment technology.

2. Experimental section

2.1. Preparation of MoS₂ nanosheets

All chemical reagents used were analytical reagent grade. The MoS_2 nanosheets were obtained by liquid-exfoliation method. Bulk MoS_2 (100 mg, Aladdin Reagent Inc.) powder was added to beaker filling with 100 mL of ethanol/water (45 : 55 vol%) as solvent. The mixed solution was sonicated for 4 h in the ultrasonic probe processor (400 W) with simultaneous cooling by ice water recirculation. Then, the dispersion was centrifuged at 3000 rpm for 1.0 h. Next, the top 3/4 portions of the supernatants were carefully collected by pipet, followed by another centrifugation of the supernatant at 4000 rpm for 1.0 h. The collected supernatant containing MoS_2 nanosheets was stored in fridge for further use.

2.2. Preparation of MoS₂ electrode

Firstly, the polyethylene glycol 4000 (5 g, $\geq$ 99.5%) was dissolved in deionized water (5 ml), followed by 2 h magnetic stirring. Then anatase TiO_2 (0.8 g, 10–25 nm, Aladdin Reagent Inc.) was added into the above solution (4 ml), and the mixture was grinded in the mortar to obtain TiO_2 slurry. Next, the slurry was doctor-bladed onto the ITO (20 × 20 mm × 1.1 mm, 6 Ω/cm^2), and the ITO substrate was annealed in air at 450 °C for 1 h with a heating rate of 5 °C/min. Secondly, the MoS_2 dispersion solution was dried at 60 °C for 12 h to obtain the MoS_2 powder. Then the powder was dissolved in 2 ml anhydrous ethanol, followed by sonication for 30 min to obtain the MoS_2 suspension. Next, the suspension was dropped on the TiO_2 based electrode at 60 °C. Finally, the ITO substrate was annealed in Ar at 300 °C for 1 h with a heating rate of 5 °C/min, and the $MoS_2/TiO_2/ITO$ electrode was obtained.

2.3. Characterization

MoS_2 crystalline phases on ITO glass were characterized by X-ray diffraction (XRD, Bruker D8 Advance). The morphology of the samples were observed using the field emission scanning electron microscope (FESEM, SU8010). The Raman spectra of different samples were performed with 532 nm excitation by the Raman spectrometer (LabRAMHR-800). High resolution transmission electron microscope (HRTEM, Tecnai G2 F30) images were used to analyze the microstructure and phases of the samples. Surface chemical composition and valence state of the samples were analyzed by the X-ray photoelectron spectroscopy (XPS, PHI 5000 VersaProbe II) with a monochromatic Al Kα ray source. The concentration of different MoS_2 suspension was quantified by measuring UV–vis absorbance with UV–vis spectrophotometer (Shimadu UV-2600). The thickness of exfoliated MoS_2 nanosheets was confirmed by Atomic Force Microscope (Dimension Icon).

2.4. Photoelectrochemical evaluation of MoS₂ photoanode

The PEC tests of different MoS_2 samples were measured by an electrochemical workstation (CHI660E, Chenhua, China) in a three-electrode system with MoS_2 as an anode, Pt foil as a cathode and Ag/AgCl as a reference. The photocurrents of the different MoS_2 photoanodes were tested under different conditions with varying electrolytes (0.1 M of Na_2SO_4, Na_2SO_3, EDTA and $Na_2C_2O_4$ (sodium oxalate) and biases (0.2 V-0.8 V) under visible light irradiation ($\geq$ 420 nm) by a 300 W Xe arc lamp with 420 nm filter (PLS-SXE300, Beijing Perfect Light Company, light intensity 95.5 mW/cm^2). Photocurrent response (i–t curves) of MoS_2 photoanode was tested with two modes: (a) light "on-off" chopped condition in 900 s; (b) continuous light irradiation for 1.0 h. Linear sweep voltamprogram (LSV) measurements were recorded from -1.0 V to 1.0 V vs Ag/AgCl reference for the electrodes in 0.1 M Na_2SO_3 solution with 50 mV/s scan rate. Electrochemical impedance spectroscopic (EIS) measurements were performed at an overpotential of 0.20 V vs. Ag/AgCl reference over frequency range from 10^{-2} to 10^5 Hz.

2.5. Photoelectrochemical conversion of pollutants

The PEC degradation of pollutants including ammonia and protein (Bovine Serum Albumin (BSA)) was tested under varied experimental conditions. The PEC degradation of ammonia (NH_3-N, 5.0–40.0 mg/ L) and protein (10.0 mg/L) was carried out with applied bias of 0.6 V in 0.1 M Na_2SO_3 electrolyte in the pH range of 4–10 utilizing MoS_2 electrode (electrode area = 1.0 cm^2). Slow and continuous air purging was used to provide more amount of oxygen into the reaction system. Ammonia nitrogen at different intervals was analysed spectrophotometrically by a Nessler reagent according to the absorption at 420 nm. Nitrate nitrogen was analysed by Ultraviolet

spectrophotometry ($A = A_{220}-A_{275}$) and nitrite nitrogen were determined by spectrophotometric method (A_{540}). The protein was determined by coomassie brilliant blue G250 method (A_{595}). The radical trapping experiments were done under the identical condition, except adding excess of iso-propyl alcohol (IPA) as hydroxyl radical scavenger. Photocatalytic ammonia conversion was done by using home prepared C_3N_4 and $BiVO_4$ photocatalysts with Na_2SO_3 and Na_2S hole scavengers. Typically, 100 mg photocatalysts were suspended into 50 ml 20 mg/L NH_3-N solution with 0.05 M Na_2SO_3 and Na_2S under continuous visible light irradiation ($\geq$ 420 nm). Multicycle ammonia degradation tests were performed by repeat use of the same MoS_2 electrode in fresh ammonia and sulfite electrolyte solution.

3. Results and discussion

3.1. Characterization of exfoliated MoS₂ nanosheets and photoanode

Liquid phase exfoliation of bulk MoS_2 has been achieved by varying the composition of liquid solvents like N-methyl-2-pyrrolidone (NMP), pure water or water/ethanol mixture, controlling the exfoliation temperature or engineering the edges of MoS_2 crystals [32–34]. However, in order to obtain monolayer or few-layer MoS_2 nanosheets, repeated long-time sonication and centrifugation processes are normally required. In this work, we tried to optimize the exfoliation parameters by varying the sonication power and time, liquid solvent composition and centrifugation speed, so as to obtain the few-layer MoS_2 nanosheets by a time-saving approach.

Firstly, we carried out the exfoliation experiment in a mixture of water/ethanol (55: 45 vol. %) with changing of sonication power and time, via monitoring the UV–vis absorbance spectra of exfoliated MoS_2 suspension. As shown in Fig. S1, the exfoliated MoS_2 nanosheets present characteristic absorption peaks located at 620 nm (B-exciton) and 670 nm (A-exciton), which can be assigned to the direct exciton transitions of MoS_2 at the K point of the Brilouin zone. The absorption intensity in the 400–800 nm region linearly increases with sonication power and time. The concentration of MoS_2 nanosheets suspension can be simply estimated using the optical absorption spectrum and the Beer-Lambert law according to the literature [34]. As summarized in Table S1, the concentration of MoS_2 nanosheets was ranged about 0.01 – 0.07 mg/L with varying sonication power and time. To get higher concentration of MoS_2 nanosheets, further experiments were done under 400 W sonication for 4 h. In addition, the solvent effect on exfoliation can be clearly seen from Fig. 1a. The optical absorptions of MoS_2 nanosheets exfoliated in NMP and mixture of ethanol/water are the highest, compared to those exfoliated in pure water and ethanol. Considering the cost and easiness for further treatment, the mixture of ethanol/water was selected for further experiments. Furthermore, centrifugation speed is a crucial parameter affecting the thickness and concentration of exfoliated MoS_2 nanosheets. According to the optical absorption characters shown in Fig. 1b, the concentrations of obtained MoS_2 nanosheets at 3000 rpm, 4000 rpm and 5000 rpm are 0.082, 0.068, and 0.024 mg/L, respectively. Larger centrifugation speed can remove the larger and thicker MoS_2 samples. The thickness of MoS_2 nanosheets obtained from different centrifugation speeds was further examined by AFM measurements. As shown in Fig. S2, the thickness of MoS_2 nanosheets obtained from 3000 rpm centrifugation was ranged about 40–100 nm. While it was dramatically reduced to less than 10 nm when the centrifugation speed was raised to 4000 rpm. The MoS_2 nanosheets with less than 5 nm thickness could be obtained by 5000 rpm centrifugation, but the concentrations of MoS_2 nanosheets was too low (0.024 mg/L). Therefore, we fixed the optimized exfoliation condition for producing few-layer MoS_2 nanosheets by using mixture of ethanol/water as dispersion solvent, 400 W sonication for 4 h and following centrifugation at 4000 rpm for 15 min. The exfoliated few-layer MoS_2 stock suspensions could be stored for about one month without precipitation, indicating the good stability of MoS_2 dispersion in mixed ethanol/water solvent.

Fig. 1c shows the Raman spectra of exfoliated MoS_2 nanosheets and bulk MoS_2 samples. The representative peaks at 380 cm^{-1} and 406 cm^{-1} correspond to the in-plane (E_{2g}) and out-of-plane (A_{1g}) lattice vibrations and no notable peaks at lower Raman shift region (< 200 cm^{-1}) could be observed, indicating that all the MoS_2 samples are composed by $2H$-MoS_2. The intensities of E_{2g} and A_{1g} peaks increased in exfoliated MoS_2 nanosheets, probably due to edge effect and increased electronic transition energies in few-layer MoS_2 [25]. Furthermore, the height of exfoliated MoS_2 nanosheets was lower than 10 nm (roughly about 15 layer) in a representative 2 μm region confirmed from the Atomic Force Microscopy (AFM) analysis (Fig. 1d). Transmission Electron Microscopy (TEM) image (Fig. 1e) clearly shows the few-layer MoS_2 nanosheets agglomerated together with dimensional size of few-hundreds nanometers, and the hexagonally symmetric structure assignable to $2H$ phase can be identified from high resolution TEM image (Fig. 1f). The crystalline structure of MoS_2 sample remains intact according to the selected area electron diffraction (SAED) pattern (inset in Fig. 1f), and the D-spacing of 0.180 nm, 0.260 nm, 0.625 nm can be estimated from the diffraction rings. These results demonstrate that the crystalline few-layer MoS_2 nanosheets were successfully prepared by our exfoliation method.

To fabricate a stable MoS_2 photoanode, a thin TiO_2 (anatase) layer was pre-deposited onto FTO electrode as supporting layer by a doctor-blade method. Then, different amounts of MoS_2 (0–4.0 mg/cm^2) were drop-casted onto the TiO_2/FTO electrode. The microstructure of MoS_2/TiO_2/FTO was investigated by scanning electron microscopy (SEM), X-ray diffraction (XRD), and X-ray photoelectron spectroscopy (XPS). The SEM images from top view clearly show that more and more MoS_2 nanosheets were attached onto particulate TiO_2 with increasing the quantity of MoS_2 from 0.5 mg/cm^2 to 4.0 mg/cm^2 (Fig. S3). The surface of TiO_2 was almost fully covered by the MoS_2 nanosheets when 4.0 mg/cm^2 MoS_2 was deposited. The SEM images from side view exhibit that the MoS_2 nanosheets were aggregated together with increased MoS_2 loading (Fig. S4). Since the top layer of TiO_2 was not flat and smooth, some portion of MoS_2 nanosheets were not fully contacted with TiO_2 particles. The chemical states of Mo and S in the prepared MoS_2/TiO_2 electrode were studied by XPS (Fig. 2a,b). The Mo 3d spectrum of MoS_2 in the electrode is similar to that of bulk MoS_2 sample, except that a slight shift towards lower binding energy is occurred. According to the analysis of the Mo 3d spectra, the majority of Mo ions existed with +4 oxidation state with $3d_{3/2}$ peak at 232.0 eV and $3d_{5/2}$ peak at 229.2 eV. Small amount of Mo^{6+} with 3d peak at 236.0 eV can be found for commercial bulk MoS_2. The portion of Mo^{6+} was reduced in the exfoliated MoS_2 electrode sample. In the S 2p core-level spectra, only a single doublet was found at 163.8 and 162.7 eV corresponding to S $2p_{1/2}$ and $2p_{3/2}$ orbitals for the commercial bulk MoS_2 sample. However, S $2p_{1/2}$ and $2p_{3/2}$ peaks are not clearly distinguished for the exfoliated MoS_2 sample, and a blue shift about 0.3 eV towards lower binding energy was also observed. The shifts of binding energy for both Mo 3d and S 2p orbitals indicate the interaction between MoS_2 and surface TiO_2 atoms. As shown in Fig. 2c, the XRD pattern of composite MoS_2/TiO_2/FTO electrode (with 3.0 mg/cm^2 MoS_2 as a representative) shows a main broad diffraction peak at 14.4° and some minor peaks 40.0° and 50.0° with relative lower intensity, which are assignable to (002), (103) and (105) planes respectively, in reference with commercial bulk MoS_2 sample. The broad and low intensity peaks of MoS_2 reflect the characters of disordered nanostructure. In addition, the diffraction peaks belong to TiO_2 and Ln_2O_3 from ITO electrode can also be clearly found.

3.2. Photoelectrochemical evaluation of MoS₂ photoanode

Fig. 3 and Fig. S5 display the photocurrent response (i–t curves) of MoS_2 electrodes with varying the amount of MoS_2 under visible light irradiation at biased potentials of 0.2-0.8 V in the presence of 0.1 M Na_2SO_3 electrolyte. The bias effect can be clearly seen by increasing the
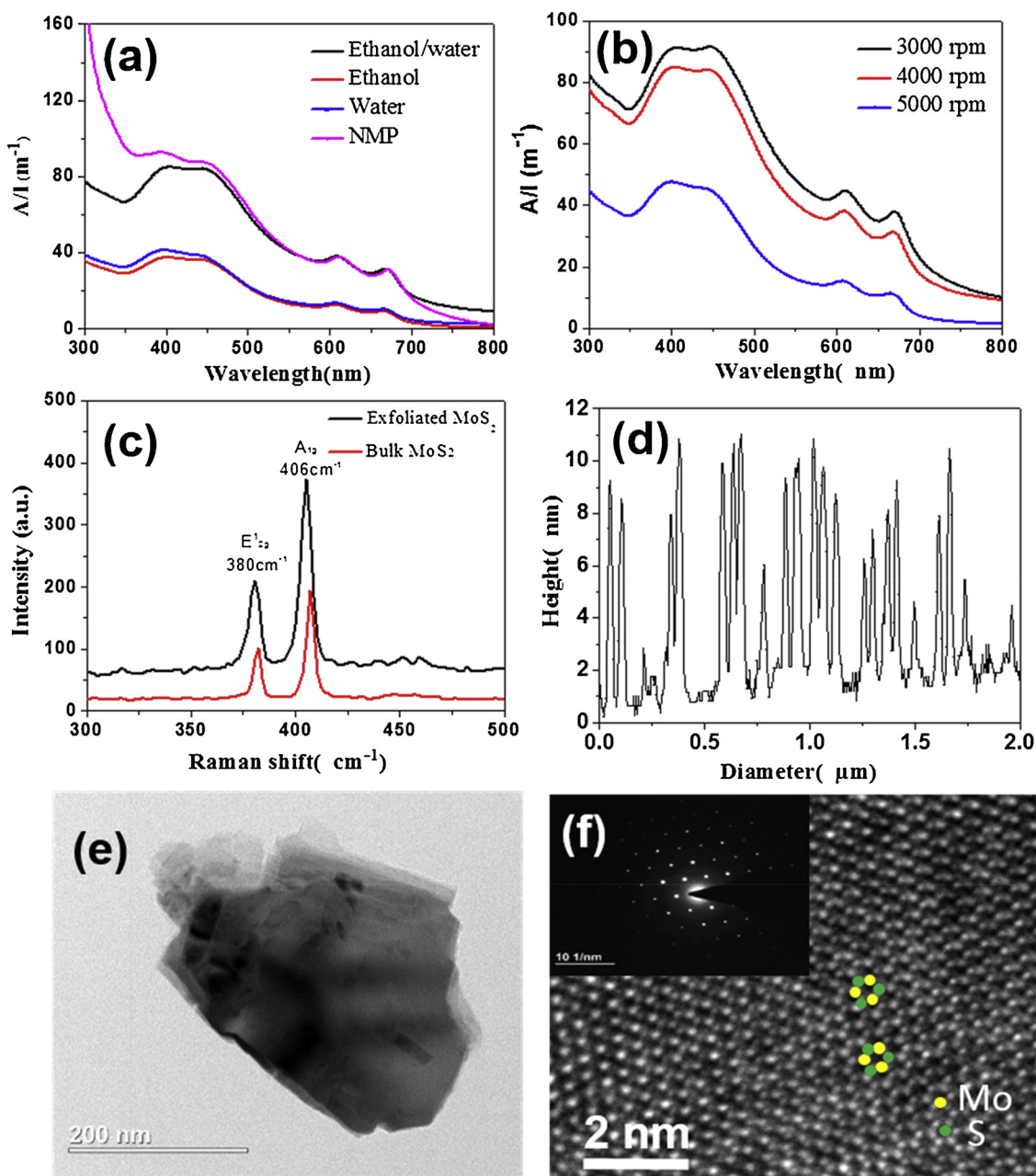
Fig. 1. (a) Optical absorption spectra of exfoliated MoS_2 nanosheets in different solvents; (b) Optical absorption spectra of exfoliated MoS_2 nanosheets with different centrifugation speeds; (c) Raman spectra of exfoliated MoS_2 nanosheets and bulk MoS_2; (d) Height profile of exfoliated MoS_2 nanosheets from AFM analysis; (e) Representative TEM image of MoS_2 nanosheets; (f) HRTEM image of MoS_2 nanosheets (SAED pattern shown in inset image).

bias potential from 0.2 V to 0.8 V, as the anodic photocurrents gradually increased for each MoS_2 electrode (Fig. S5). The MoS_2 electrode with 3.0 mg/cm^2 loading exhibited the highest anodic photocurrents at each bias condition. However, it was generally observed that the rise and decay of photocurrents are much slower for all the MoS_2 electrodes during the repeated light "on-off" process. For the chronoamperometric experiments tested in a longer time scale, the photocurrents even gradually increased for all the MoS_2 electrodes during the continuous 1 h irradiation (Fig. 3b). The irregular microstructure of deposited MoS_2 nanosheets aggregates, as evidenced from the previous SEM observation, leads to poor interface contact between MoS_2 nanosheets and TiO_2 particles, which might result in the slower inwards charge transfer from MoS_2 to TiO_2 under visible light irradiation. This effect is more pronounced in higher MoS_2 loading (2.0–4.0 mg/cm^2) samples than those in lower MoS_2 loading samples (0.5–1.0 mg/cm^2). To further improve

the photoelectrochemical performance, the electrode interface engineering should be adopted. In addition, the photocurrents were significantly improved by 40–50 folds using 0.1 M sodium sulfite (Na_2SO_3) as electrolytes compared to 0.1 M methanol, 0.1 M sodium sulfate (Na_2SO_4), 0.1 M sodium ethylene diamine tetraacetate (EDTA), or 0.1 M sodium oxalate ($Na_2C_2O_4$) electrolytes (Fig. S6). Only Na_2SO_3 serves as efficient hole scavenger to enhance photocurrent generation.

The linear sweep voltammetry (LSV) measurements were conducted in 0.1 M Na_2SO_3 with 50 mV/s scan rate for the MoS_2 electrode under dark and light illumination conditions (Fig. 3c). The anodic photocurrents can be clearly observed from the potential above 0.25 V (vs. Ag/AgCl) under visible light irradiation compared to dark currents. The onset potential of MoS_2 was clearly shifted ~0.1 V under light illumination. To further pinpoint the charge transfer characters of the MoS_2 electrode, the charge transfer kinetics were evaluated by
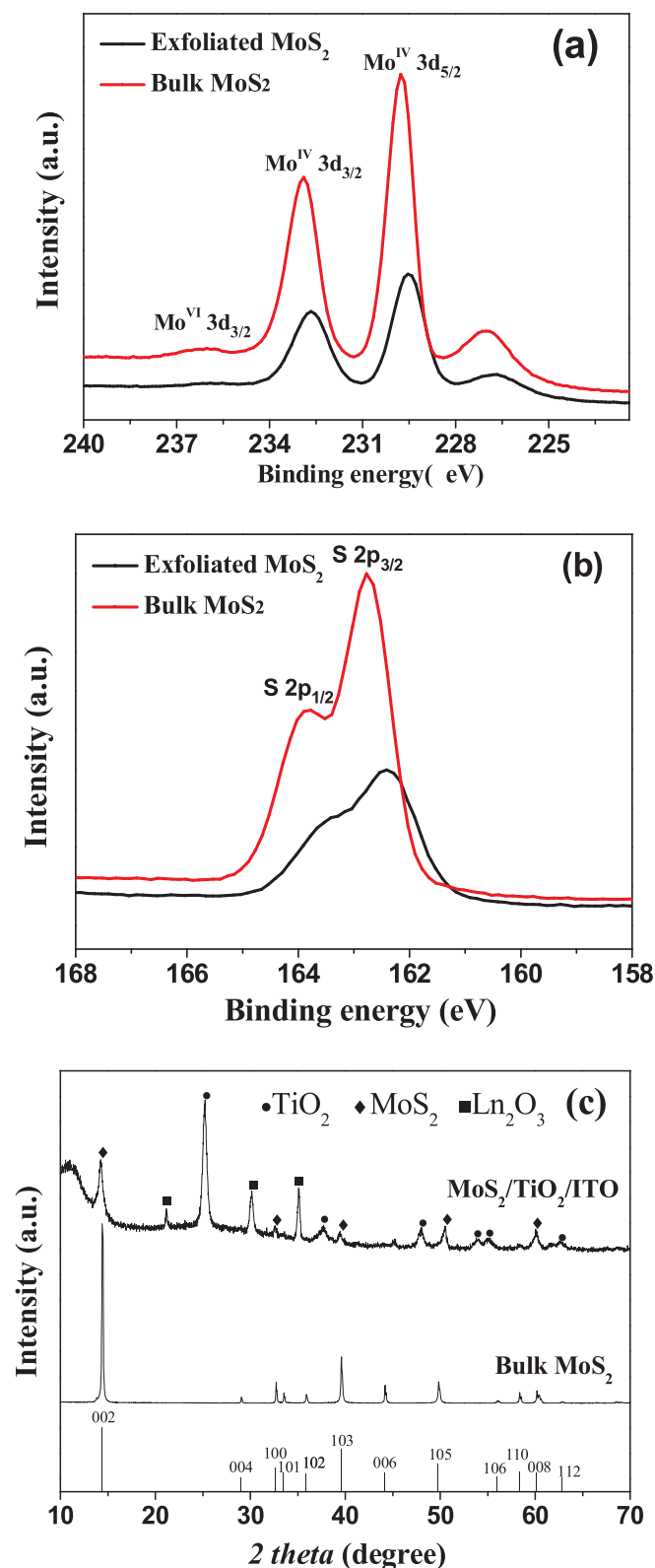
Fig. 2. (a) Mo 3d XPS spectra, (b) S 2p XPS spectra and (c) XRD pattern of MoS$_2$/TiO$_2$/ITO electrode in reference with bulk MoS$_2$ sample.

electrochemical impedance spectroscopy (EIS) Nyquist analysis. In the Nyquist plot shown in Fig. 3d, the MoS$_2$ under light illumination displayed much narrower semicircle diameter than that under dark condition, implying the resistance of the carriers' migration across the interface of catalyst/solution was decreased under light illumination.

3.3. Photoelectrochemical removal of ammonia in the presence of sulfite

Fig. 4 displays the time courses of ammonia conversion with varying experimental parameters including dissolved oxygen concentration, pH, bias potentials and concentration of ammonia during the photoelectrochemical (PEC) and electrochemical (EC) processes. Fig. 4a shows the pH effect on the ammonia nitrogen removal in the MoS$_2$ based PEC system (3.0 mg/cm^2 MoS$_2$ electrode, 0.1 M Na$_2$SO$_3$ electrolyte, 0.6 V bias vs. Ag/AgCl, ammonia nitrogen = 10.0 mg/L). The solution pH determines the existence state of ammonia nitrogen (pKa (NH$_4^+$) = 9.24 at 25 °C) in aqueous solution, and thus is a key parameter influencing the PEC degradation rates of ammonia nitrogen. The pH dependent characteristics for removal of ammonia nitrogen was clearly observed as shown in the Fig. 4a. At neutral or acidic condition, the concentration of ammonia nitrogen was hardly reduced after 6 h reaction during EC or PEC processes, whereas the PEC degradation was markedly enhanced at pH 10 and pH 12. These results indicate that photocatalysis mainly contributes to the ammonia nitrogen conversion compared to the electrocatalysis. The conversion of ammonia nitrogen follows pseudo first-order kinetics as shown in Fig. 5, and rate constants (k) increased from 0.016 h^{-1} to 0.282 h^{-1} from pH 4 to 12 as shown in the kinetic curves (Fig. 5a). The pH dependent degradation behaviour has been well documented in previous literature. In most cases, the photocatalytic conversion of ammonia nitrogen by different kinds of photocatalysts was favored at basic condition (e.g. pH ∼ 10), except that Zhou's group reported that the degradation rate was enhanced at lower pH in combined PEC-chlorine system [20].

The bias effect was further evaluated for the PEC removal of ammonia at pH 10 in the presence of 0.1 M Na$_2$SO$_3$. As shown in Fig. 4b, both EC and PEC conversion efficiencies were gradually improved with increasing the applied anodic potentials. The PEC ammonia conversion efficiencies within 6 h were about 59.0%, 76.7% and 84.8%, and the conversion rate constants k were calculated about 0.176 h^{-1}, 0.268 h^{-1} and 0.339 h^{-1} for the applied bias potential of 0.4 V, 0.6 V and 0.8 V, respectively (Fig. 5b). The PEC performance was not significantly improved when the applied bias from 0.6 V to 0.8 V, especially during the initial 3 h reaction. From energy consuming, economic cost and electrode stability concern, employing relatively lower bias potential is preferred for practical application.

Fig. 4c shows the dissolved oxygen effect on the PEC removal of ammonia nitrogen (0.6 V bias, pH = 10), and it was found that ammonia nitrogen removal was only slightly enhanced by pumping air into the reactor for providing more amount of oxygen during the EC process. In contrast, the ammonia removal was markedly enhanced from about 60.7% (without pumping air) to 77.0% (with pumping air) during the PEC process. Furthermore, the conversion rate constants k were calculated about ∼0.168 and 0.268 h^{-1} for the tests without and with air pumping, respectively (Fig. 5c). We also conducted the PEC tests with increasing the concentration of ammonia nitrogen from 5.0 mg/L to 40.0 mg/L under the optimized condition. As shown in Fig. 4d, the overall PEC conversion ratios in 6 h were slightly reduced from 81.7% for 5 mg/L to 66.8% for 40 mg/L, and the conversion rate constants were about 0.300 h^{-1}, 0.268 h^{-1}, 0.212 h^{-1} and 0.201 h^{-1} with increasing the concentration of ammonia nitrogen from 5 mg/L to 40 mg/L (Fig. 5d).

As shown in Fig. 6, only moderate level of nitrate was found from the reacted solution and no nitrite was found. This indicates that ammonia was selectively transformed into N$_2$. This is quite different with the cases of hydroxyl radicals mediated oxidation, in which nitrate and nitrite anions are found as the main products. The selective NH$_3$ to N$_2$ conversion in this work is similar to the chlorine radical species mediated PEC conversion of ammonia nitrogen reported in the literature [20]. Practically, the complete removal of ammonia nitrogen from water is favorable for the wastewater treatment.

The photocorrsion of sulfide based photocatalysts impedes their widespread use for practical applications, thus sacrificial agents such as
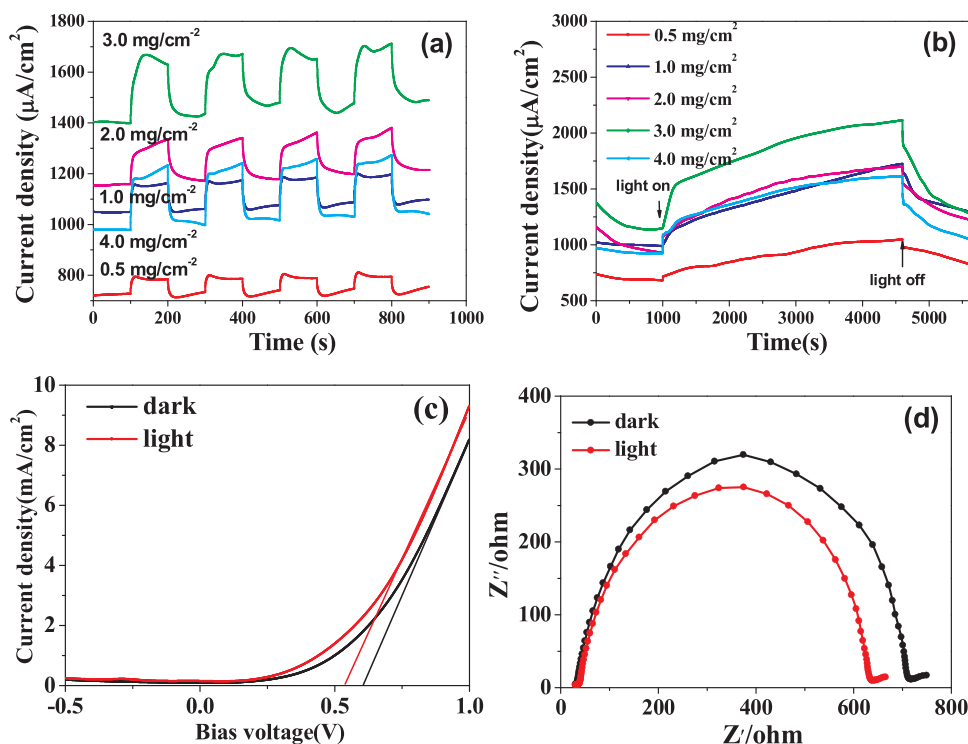
Fig. 3. Photocurrent response (i–t curves) of MoS$_2$ photoanode with loading different amount of MoS$_2$ nanosheets with 0.6 V bias vs. Ag/AgCl under visible light irradiation (a) light "on-off" chopped condition in 900 s; (b) continuous light irradiation for 1 h. (c) linear sweep voltammetry (LSV) and (d) electrochemical impedance spectroscopy (EIS) analysis of MoS$_2$ photoanode (3.0 mg/cm^2) under dark and visible light irradiation.
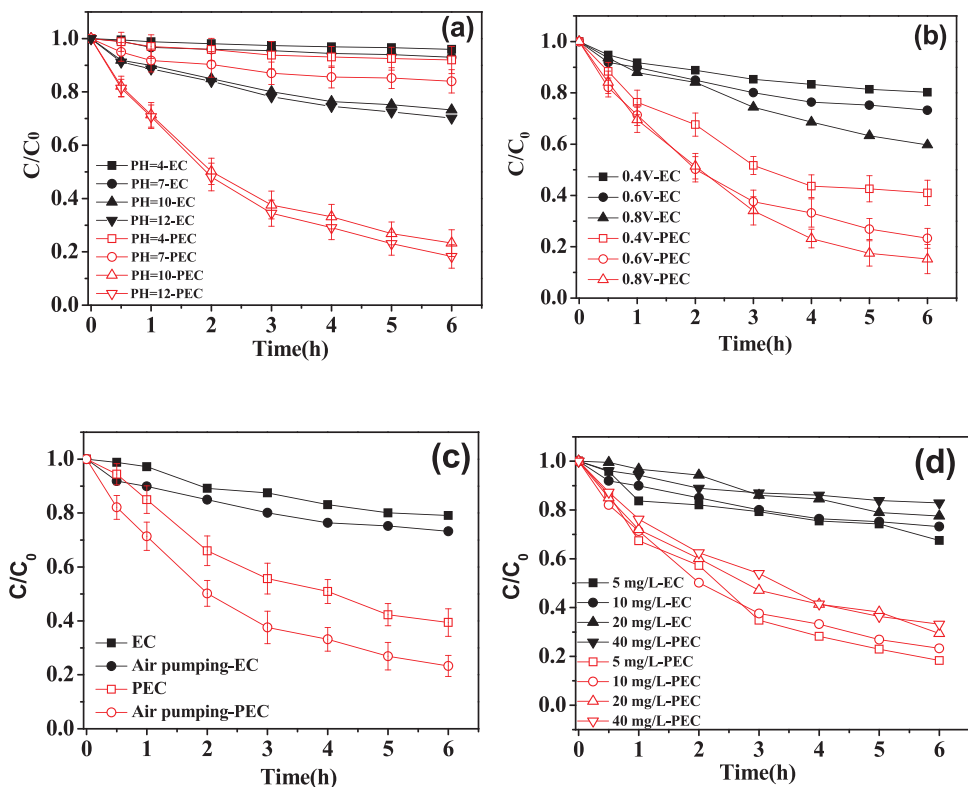

Fig. 4. Ammonia nitrogen degradation by the electrochemical (EC) and photoelectrochemical (PEC) process with varied experimental conditions. (a) pH effect; (b) anodic potential effect; (c) dissolved oxygen concentration effect; (d) ammonia nitrogen concentration effect. Initial experimental conditions without specific notification: [NH$_3$-N] = 10 mg/L, [Na$_2$SO$_3$] = 0.1 M, pH = 10, applied bias 0.6 V vs Ag/AgCl, electrode area = 1.0 cm^2, with ~3.0 mg MoS$_2$ nanosheets.

sulfide and sulfite ions are used in most cases to overcome this issue. To further examine stability of the MoS$_2$ electrode in the present system, multicycle PEC degradation of ammonia was performed and MoS$_2$ sample upon the catalytic use was further analyzed by XPS. As shown in Fig. 7a, the MoS$_2$ electrode did not exhibit significant loss of activity after five cycles. Furthermore, the XPS spectra of Mo element of MoS$_2$ sample before and after catalytic use had little change, in addition to the slightly reduced peak intensities (Fig. 7b). However, the S 2 $p_{1/2}$

peak was disappeared after oxidation, indicating that the sulfide oxidation is the main factor determining the stability of MoS$_2$ electrode (Fig. 7c). The sulfite electrolyte has to be used to prevent the photocorrsion of metal sulfide electrode.

3.4. Mechanism of oxysulfur radicals mediated ammonia removal

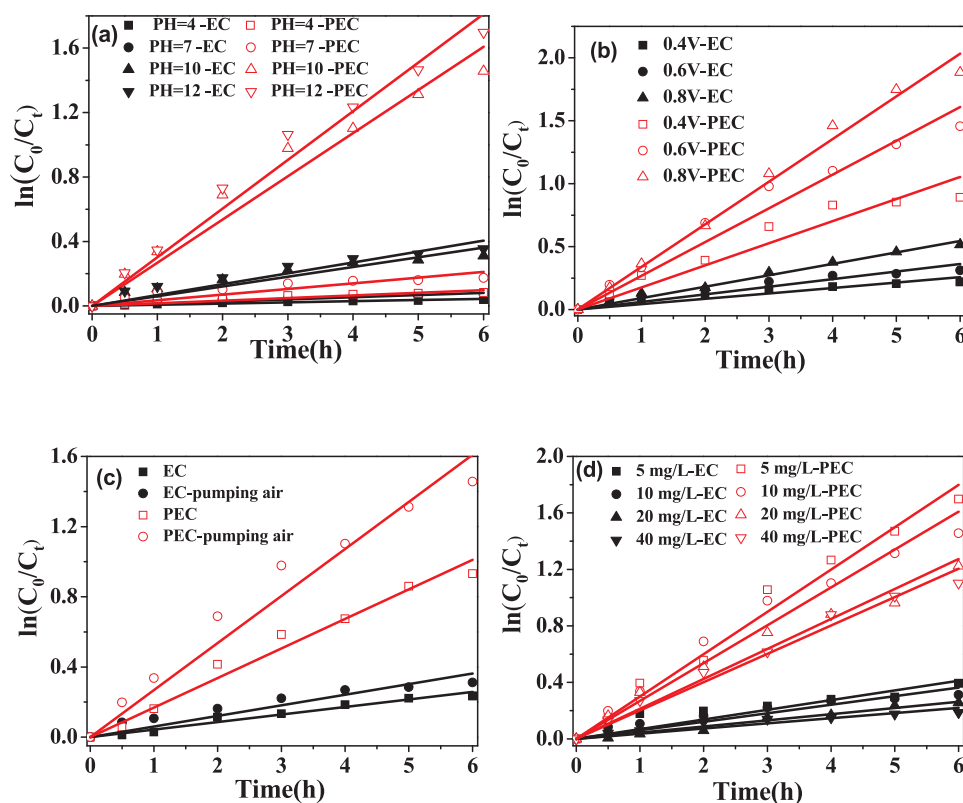To verify the role of each radical species in the PEC system, we

Fig. 5. Pseudo first-order reaction kinetics of ammonia nitrogen degradation by the electrochemical (EC) and photoelectrochemical (PEC) process with varied experimental conditions. (a) pH effect; (b) anodic potential effect; (c) dissolved oxygen concentration effect; (d) ammonia nitrogen concentration effect.

carried out a series of radical quenching and control experiments. As shown in Fig. 8a, with adding excess of hydroxyl radical scavenger (isopropyl alcohol, IPA), only slight reduction of conversion efficiencies for both PEC and EC systems was observed. This indicates that $^{\cdot}OH$ was not main oxidant for ammonia conversion. The superoxide radicals $O_2^{\cdot-}$ could be generated by electron reduction of dissolved oxygen at cathode. The oxygen effects as shown in Figs. 4c and 8 b indicate that $O_2^{\cdot-}$ was also not main oxidant, since there was negligible difference when varying the concentration of dissolved O_2 in the reactor during the EC process. In addition, the hole mediated direct oxidation was also excluded from this system, since SO_3^{2-} is an efficient hole scavenger. Thus, we believe that the active species responsible for ammonia

conversion are oxysulfur radicals, and their capability of reaction with other pollutants has been reported in the literature [35–37]. Thermodynamically, the $SO_3^{\cdot-}$ could be generated from oxidation of SO_3^{2-} by valence band holes from nanostructured MoS_2 under visible light irradiation, because the redox potential of $SO_3^{\cdot-}/SO_3^{2-}$ couple is 1.2 V vs. SHE [36], which is much lower than the valence band position of MoS_2 (1.3–1.5 V vs. SHE) [27]. In aerobic condition, the generated $SO_3^{\cdot-}$ radicals would be easily oxidized into $SO_5^{\cdot-}$ and then $SO_4^{\cdot-}$ radicals by dissolved O_2. The oxidation of $SO_3^{\cdot-}$ by O_2 is extremely fast, the rate constant is about $1–2.3 \times 10^9 \ M^{-1}s^{-1}$, and $^{\cdot}OH$ can also be indirectly generated by $SO_4^{\cdot-}$ grabbing an electron from hydroxide in alkaline pH with relative slower reaction rate ($1.4 \times 10^7 \ M^{-1}s^{-1}$) [38].
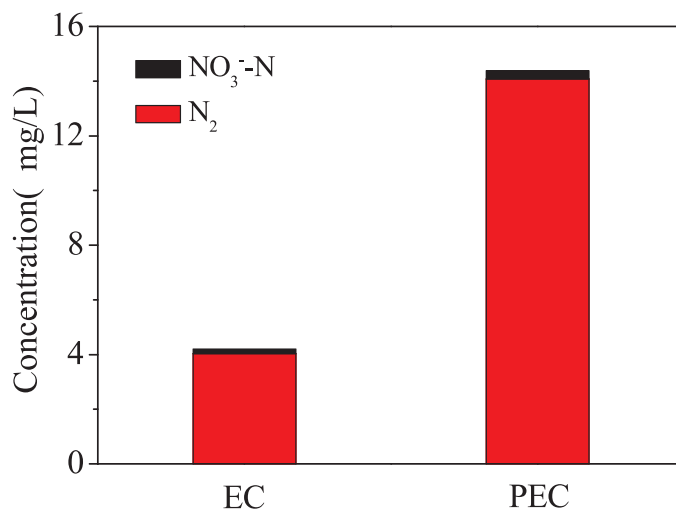

Fig. 6. Products analysis of ammonia conversion during the electrochemical (EC) and photoelectrochemical (PEC) process. Initial experimental conditions: [NH₃-N] = 20 mg/L, [Na₂SO₃] = 0.1 M, pH = 10, applied bias 0.6 V vs. Ag/AgCl.
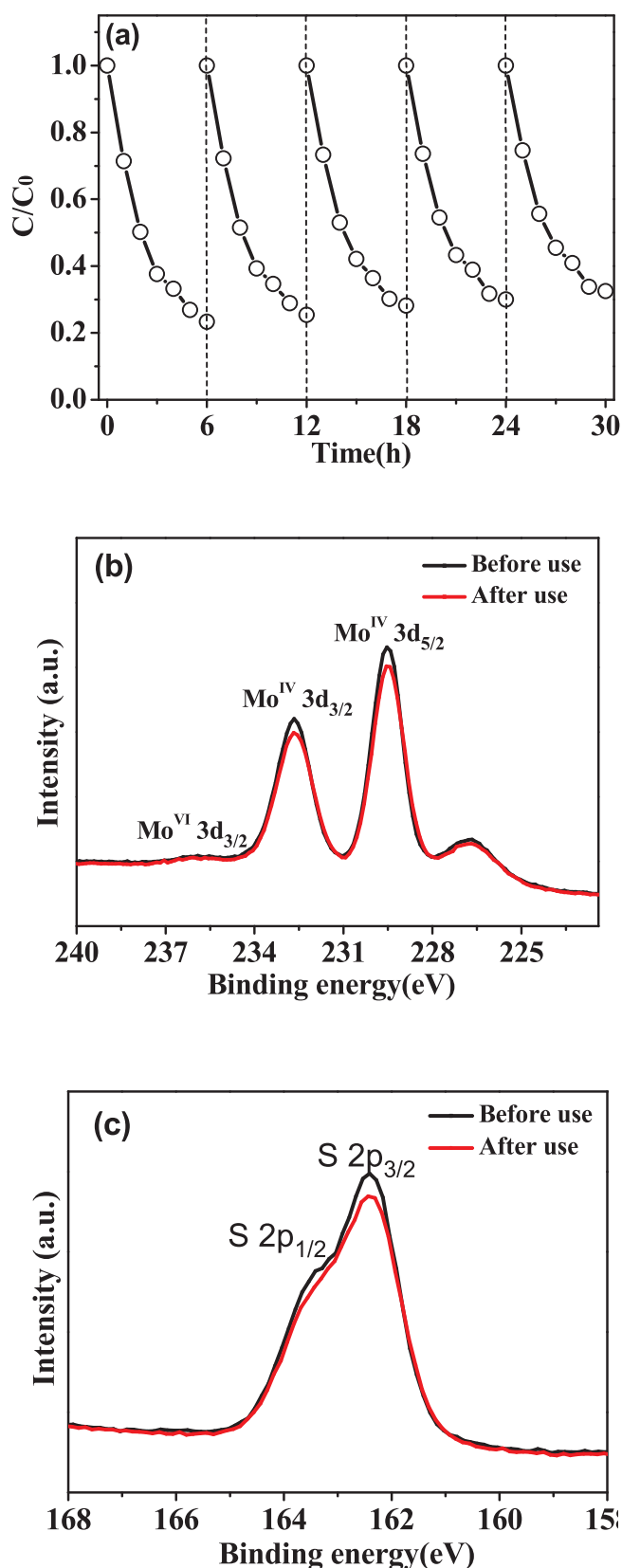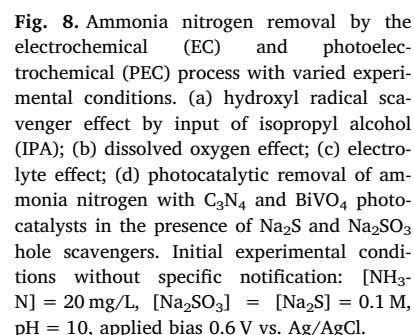
Fig. 7. (a) Multicycle tests of PEC degradation of ammonia with MoS$_2$ electrode; (b) Mo 3d XPS spectra and (c) S 2p XPS spectra of MoS$_2$ sample upon PEC oxidation.

Thus, the coexisting oxysulfur radicals are potential main oxidants of ammonia, which can be evidenced from the experimental investigation. Firstly, the influence of O$_2$ is negligible in EC process, but O$_2$ plays an important role in PEC conversion process (conversion efficiency improved about 20%) as shown in Figs. 4c and 8 b. One possibility accounting for this is that SO$_4^{\cdot-}$ and SO$_5^{\cdot-}$ radicals generated by O$_2$ oxidation of SO$_3^{\cdot-}$ participate the ammonia conversion. Although SO$_3^{\cdot-}$ radicals have much less oxidation potentials and reaction rate constants against most compounds than those of SO$_4^{\cdot-}$ and SO$_5^{\cdot-}$, their steady-state concentrations are notably much larger than those of SO$_4^{\cdot-}$ and SO$_5^{\cdot-}$. Therefore, the kinetic contribution of SO$_3^{\cdot-}$ radicals toward substrate oxidation can be compensated. Secondly, both Na$_2$SO$_3$ and Na$_2$S can be efficient hole scavengers of MoS$_2$ photocatalyst. If other radical species rather than oxysulfur radicals are corresponding oxidants, the conversion of ammonia should be similar with Na$_2$SO$_3$ and Na$_2$S electrolyte. However, ammonia conversion was much less efficient in the presence of Na$_2$S electrolyte (Fig. 8c). In contrast, the ammonia conversion rate was linearly dependent on the concentration of Na$_2$SO$_3$ (Fig. S7). Thirdly, we performed heterogeneous ammonia conversion experiments using C$_3$N$_4$ and BiVO$_4$ photocatalysts in the presence of Na$_2$SO$_3$ or Na$_2$S hole scavengers as shown in Fig. 8d. Since both valence band holes of C$_3$N$_4$ and BiVO$_4$ can be efficiently consumed by Na$_2$SO$_3$ or Na$_2$S, the oxysulfur or sulfur radicals can be produced as well. As expected, ammonia conversion was only efficient in the presence of Na$_2$SO$_3$. The universality of oxysulfur radicals mediated ammonia conversion is clearly demonstrated according to these results.

There are several possible pathways dinitrogen is electrochemically or photochemically reduced to ammonia at a heterogeneous surface [39]. Herein, the ammonia oxidation to dinitrogen might be realized via the reversed pathways. The two possible pathways accounting for ammonia conversion by oxysulfur radicals were proposed as shown in Scheme 1.The absorption of ammonia onto MoS$_2$ surface (mainly on Mo atom sites) facilitates the further proton coupled electron transfer (PCET) process. The possible radical intermediates including *NH$_2$, *NH, *N, *NH$_2$NH$_2$, *NHNH$_2$, *NHNH, *NNH and *N$_2$ are formed by the oxidation of SO$_x^{\cdot-}$. In pathway (a), N−N bond coupling is realized by addition of two *NH$_2$ species with formation of *NH$_2$NH$_2$ species, further deprotonation of which by the oxidation of SO$_x^{\cdot-}$ during the PCET process generates dinitrogen eventually. On the other hand, in pathway (b), *N species could be firstly generated by continuous deprotonation of *NH$_3$, and N−N bond coupling can be formed by addition of *NH$_2$ to the *N with production of *NNH$_2$ species. After further deprotonation, N$_2$ molecule can be produced.
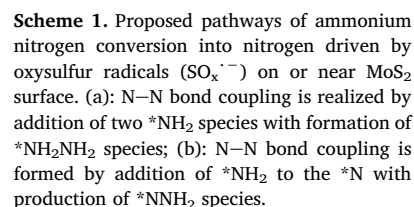
3.5. Applications

The AOPs based on oxysulfur radicals (SO$_3^{\cdot-}$, SO$_4^{\cdot-}$ and SO$_5^{\cdot-}$) have been increasingly studied as an alternative of $^{\cdot}$OH radicals for pollutants treatment. Unlike $^{\cdot}$OH radicals that could be produced by a variety of approaches, oxysulfur radicals are normally obtained through chemical activation of persulfates or sulfite catalyzed by transitional metal ions such as iron, cobalt, copper, nickel, chromium, manganese, etc or input of high-energy for dissociation [16,35–37,39–41]. Currently, the well-established homogenous transition metal catalyzed activation system suffers serious issues such as metal ion deactivation and post sludge disposal. Additionally, requirement for massive input of chemical agents dramatically increases the cost of operation, complexity of separation, and potential risk of secondary pollution. Therefore, it is crucial to develop approaches by which oxysulfur radicals can be generated without consuming extrinsic chemicals. Upgrading homogeneous reaction into heterogeneous reaction has been adopted to address the issues mentioned above. For instance, it has been demonstrated that sulfite and persulfates activation can be achieved by semiconductor photocatalysis such as BiOCl, surface modified TiO$_2$ and nanodiamonds photocatalysts under visible light irradiation [42–45]. Compared to the heterogeneous activation of sulfite and persulfates,

Fig. 8. Ammonia nitrogen removal by the electrochemical (EC) and photoelectrochemical (PEC) process with varied experimental conditions. (a) hydroxyl radical scavenger effect by input of isopropyl alcohol (IPA); (b) dissolved oxygen effect; (c) electrolyte effect; (d) photocatalytic removal of ammonia nitrogen with C_3N_4 and $BiVO_4$ photocatalysts in the presence of Na_2S and Na_2SO_3 hole scavengers. Initial experimental conditions without specific notification: [NH_3-N] = 20 mg/L, [Na_2SO_3] = [Na_2S] = 0.1 M, pH = 10, applied bias 0.6 V vs. Ag/AgCl.

PEC system shows more advantages in practical water treatment process, in aspects of immobilization of photocatalyst and efficient photogenerated charge separation. Sulfite and ammonia are ubiquitous pollutants in different kinds of industrial wastewater, such as the wastewater from ammonia absorption of SO_2 exhaust gas for desulfurization of combustion smoke. We attempted to develop a new strategy to specifically and effectively convert ammonia nitrogen utilizing oxysulfur radicals based AOPs via in situ PEC activation of sulfite.

In addition to the in situ generated oxysulfur radicals, hydroxyl radicals indirectly generated can also participate in the degradation of pollutes. This provides a new protocol in the design of new AOPs, where oxysulfur radicals can work together with hydroxyl radicals. In addition to the ammonia nitrogen removal, the present PEC system can also effectively degrade different kind of pollutant such as protein as shown in Fig. 9, in which ·OH might be the dominant oxidant. This result appears to be more attractive, since there will be multiple inorganic,

organic and biological pollutants coexisted in wastewater, and the co-generation of different types of oxidative radical species can realize simultaneous pollutants degradation and detoxification.

4. Conclusions

In summary, this study offers a proof-in-concept demonstration of MoS_2 based PEC activation of sulfite for producing oxysulfur radicals that can efficiently convert ammonia nitrogen to dinitrogen, which is considered as an ideal conversion path in terms of complete removal of ammonia nitrogen. The advantages of the present MoS_2-based PEC activation system include: (i) MoS_2 is composed by earth-abundant elements and the fabrication of nanostructured MoS_2 photoanode is quite simple and up-scalable. (ii) Nanostructured MoS_2 with a narrow band-gap can efficiently utilize the visible light part in the solar irradiation spectrum, and the valence band position of MoS_2 is suitable for
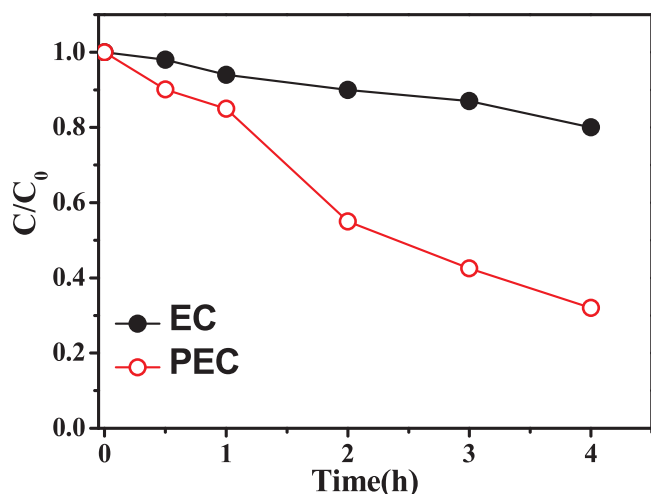

Scheme 1. Proposed pathways of ammonium nitrogen conversion into nitrogen driven by oxysulfur radicals ($SO_x^{\cdot-}$) on or near MoS_2 surface. (a): N−N bond coupling is realized by addition of two *NH_2 species with formation of *NH_2NH_2 species; (b): N−N bond coupling is formed by addition of *NH_2 to the *N with production of *NNH_2 species.

Fig. 9. Bovine Serum Albumin (BSA) degradation by MoS_2 –Na_2SO_3 system in photoelectrochemical and electrochemical processes. Initial experimental conditions: [BSA] = 10 mg/L, [Na_2SO_3] = 0.1 M, pH = 10, applied bias 0.6 V vs. Ag/AgCl.

oxidizing SO_3^{2-} to generate oxysulfur radicals. (iii) It is a "one stone two birds" strategy to utilize SO_3^{2-} as hole scavenger for improving stability of MoS_2 electrode by inhibiting photo-corrosion and as precursor of oxysulfur radicals in the meantime. Future work includes, but not limited to, the modification of MoS_2 photoanode to enhance the photo charge separation and solar light utilization efficiency; fundamental study on the mechanisms for radical formation and reaction; systematic investigation on the impact of coexisting ion species; the selectivity during multi-pollutants degradation test and the optimization on the design of PEC-sulfite based AOPs system for more practical applications.

Notes

The authors declare no competing financial interest

Appendix A. Supplementary data

Supplementary material related to this article can be found, in the online version, at doi:https://doi.org/10.1016/j.apcatb.2018.11.061.

References

[1] H.A. Hasan, S.R.S. Abdullah, S.K. Kamarudin, N.T. Kofli, N. Anuar, Kinetic evaluation of simultaneous COD, ammonia and manganese removal from drinking water using a biological aerated filter system, Sep. Purif. Technol. 130 (2014) 56–64.
[2] H. Huang, L. Huang, Q. Zhang, Y. Jiang, L. Ding, Chlorinationi decomposition of struvite and recycling of its product for the removal of ammonium-nitrogen from landfill leachate, Chemosphere 136 (2015) 289–296.
[3] X. Li, Y. Yuan, Y. Huang, H. Liu, Z. Bi, Y. Yuan, P. Yang, A novel method of simultaneous NH_4^+ and NO_3^- removal using Fe cycling as a catalyst: feammox coupled with NAFO, Sci. Total Environ. 631–632 (2018) 153–157.
[4] H. Zollig, C. Fritzsche, E. Morgenroth, K.M. Udert, Direct electrochemical oxidation of ammonia on graphite as a treatment option for stored source separated urine, Water Res. 69 (2015) 284–294.
[5] W.A. Tarpeh, J.M. Barazesh, T.Y. Cath, K.L. Nelson, Electrochemical stripping to recover nitrogen from source-separated urine, Environ. Sci. Technol. 52 (2018) 1453–1460.
[6] S.Q. Liu, X.L. Zhu, Y. Zhou, Z.D. Meng, Z.G. Chen, C.B. Liu, F. Chen, Z.Y. Wu, J.C. Qian, Smart photocatalytic removal of ammonia through molecular recognition of zinc ferrite reduced graphene oxide hybrid catalyst under visible light irradiation, Catal. Sci. Technol. 7 (2017) 3210–3217.
[7] R. Wang, T. Xie, Z. Sun, T. Pu, W. Li, J.P. Ao, Graphene quantum dot modified g-C_3N_4 for enhanced photocatalytic oxidation of ammonia performance, RSC Adv. 7 (2017) 51687–51694.
[8] D. Sun, W. Sun, W. Yang, Q. Li, J.K. Shang, Efficient photocatalytic removal of aqueous NH_4^+-NH_3 by palladium-modified nitrogen-doped titanium oxide nanoparticles under visible light illumination, even in weak alkaline solutions, Chem. Eng. J. 264 (2015) 728–734.
[9] H. Wang, Y. Su, H. Zhao, H. Yu, S. Chen, Y. Zhang, X. Quan, Photocatalytic oxidation of aqueous ammonia using atomic single layer graphitic-C_3N_4, Environ. Sci. Technol. 48 (2014) 11984–11990.
[10] Z. Bian, F. Cao, J. Zhu, H. Li, Plant uptake-assisted round-the-clock photocatalysis for complete purification of aquaculture wastewater using sunlight, Environ. Sci. Technol. 49 (2015) 2418–2424.
[11] H. Kominami, H. Nishimune, Y. Ohta, Y. Arakawa, T. Inaba, Photocatalytic hydrogen formation from ammonia and methyl amine in an aqueous suspension of metal-loaded titanium(IV) oxide particles, Appl. Catal. B: Environ. 111–112 (2012) 297–302.
[12] M.V. Dozzi, S. Brocato, G. Marra, G. Tozzola, L. Meda, E. Selli, Aqueous ammonia abatement on Pt- and Ru-modified TiO2: selectivity effects of the metal nanoparticles deposition method, Catal. Today 287 (2017) 148–154.
[13] S. Shibuya, Y. Sekine, I. Mikami, Influence of pH and pH adjustment conditions on photocatalytic oxidation of aqueous ammonia under airflow over Pt-loaded TiO2, Appl. Catal. A Gen. 496 (2015) 73–78.
[14] M. Altomare, G.L. Chiarello, A. Costa, M. Guarino, E. Selli, Photocatalytic abatement of ammonia in nitrogen-containing effluents, Chem. Eng. J. 191 (2012) 394–401.
[15] H.H. Ou, M.R. Hoffman, C.H. Liao, J.H. Hong, S.L. Lo, Photocatalytic oxidation of aqueous ammonia over platinized microwave-assisted titanate nanotubes, Appl. Catal. B: Environ. 99 (2010) 74–80.
[16] G. Liu, S. You, Y. Tan, N. Ren, In-situ photochemical activation of sulfate for enhanced degradation of organic pollutants in water, Environ. Sci. Technol. 51 (2017) 2339–2346.
[17] J.T. Jasper, O.S. Shafaat, M.R. Hoffmann, Electrochemical transformation of trace organic contaminants in latrine wastewater, Envrion. Sci. Technol. 50 (2016) 10198–10208.
[18] J.T. Jasper, Y. Yang, M.R. Hoffmann, Toxic byproduct formation during electrochemical treatment of latrine wastewater, Envrion. Sci. Technol. 51 (2017) 7111–7119.
[19] Y. Yang, J. Shin, J.T. Jasper, M.R. Hoffmann, Multilayer heterojunction anodes for saline wastewater treatment: design strategies and reactive species generation mechanisms, Environ. Sci. Technol. 50 (2016) 8780–8787.
[20] Y. Zhi, J. Bai, J. Li, T. Luo, L. Qiao, Q. Zeng, B. Zhou, Highly selective transformation of ammonia nitrogen to N_2 based on a novel solar-driven photoelectrocatalytic-chlorine radical reactions system, Water Res. 125 (2017) 512–519.
[21] B. Zhou, J. Bai, J. Li, H_2O_2 assisted photoelectrocatalytic degradation of diclofenac sodium at g-C_3N_4/BiVO4 photoanode under visible light irradiation, Science 351 (2016) 30–31.
[22] S. Liu, X. Zhao, H. Zeng, Y. Wang, M. Qiao, Enhancement of photoelectrocatalytic degradation of diclofenac with persulfate activated by Cu cathode, Chem. Eng. J. 320 (2017) 168–177.
[23] R.C. Pawar, Y. Pyo, S.H. Ahn, C.S. Lee, Photoelectrochemical properties and photodegradation of organic pollutants using hematite hybrids modified by gold nanoparticles and graphitic carbon nitride, Appl. Catal. B: Environ. 176–177 (2015) 654–666.
[24] Y. Cong, J. Wang, H. Jin, X. Feng, Q. Wang, Enhanced photoelectrocatalytic activity of a novel Bi2O3–BiPO4 composite electrode for the degradation of refractory pollutants under visible light irradiation, Ind. Eng. Chem. Res. 55 (2016) 1221–1228.
[25] F.M. Pesci, M.S. Sokolikova, C. Grotta, P.C. Sherrell, F. Reale, K. Sharda, N. Ni, P. Palczynski, MoS_2/WS2 Heterojunction for photoelectrochemical water oxidation, ACS Catal. 7 (2017) 4990–4998.
[26] M.L. Tsai, S.H. Su, J.K. Chang, D.S. Tsai, C.H. Chen, C.I. Wu, L.J. Li, L.J. Chen, J.H. He, Monolayer MoS_2 heterojunction solar cells, ACS Nano 8 (2014) 8317–8322.
[27] C. Liu, D. Kong, P. Hsu, H. Yuan, H. Lee, Y. Liu, H. Wang, S. Wang, K. Yan, D. Lin, P.A. Maraccini, K.M. Parker, A.B. Boehm, Y. Cui, Rapid water disinfection using vertically aligned MoS_2 nanofilms and visible light, Nature Nanotechnol. 11 (2016) 1098–1105.
[28] Q. Ding, B. Song, P. Xu, S. Jin, Efficient electrocatalytic and photoelectrochemical hydrogen generation using MoS_2 and related compounds, Chem. 1 (2016) 699–726.
[29] Y. Chen, G. Tian, Y. Shi, Y. Xiao, H. Fu, Hierarchical MoS_2/Bi2MoO6 composites with synergistic effect for enhanced visible photocatalytic activity, Appl. Catal. B: Environ. 164 (2015) 40–47.
[30] X. Meng, Z. Li, H. Zeng, J. Chen, Z. Zhang, MoS_2 quantum dots-interspersed Bi2WO6 heterostructures for visible light-induced detoxification and disinfection, Appl. Catal. B: Environ. 210 (2017) 160–172.
[31] R. Tang, R. Yin, S. Zhou, T. Ge, Z. Yuan, L. Zhang, L. Yin, Layered MoS_2 coupled MOFs-derived dual-phase TiO2 for enhanced photoelectrochemical performance, J. Mater. Chem. A. 5 (2017) 4962–4971.
[32] K.G. Zhou, N.N. Mao, H.X. Wang, Y. Peng, H.L. Zhang, A mixed-solvent stategy for efficient exfoliation of inorganic graphene analogues, Angew. Chem. 123 (2011) 11031–11034.
[33] J. Kim, S. Kwon, D.H. Cho, B. Kang, H. Kwon, Y. Kim, S.O. Park, G.Y. Jung, E. Shin,

W. Kim, H. Lee, G.H. Ryu, M. Choi, T.H. Kim, J. Oh, S. Park, S.K. Kwak, S.W. Yoon, D. Byun, Z. Lee, C. Lee, Direct exfolation and dispersion of two-dimensional materials in pure water via temperature control, Nature Commun. 6 (2015) 8294–8302.

[34] X. Hai, K. Chang, H. Pang, M. Li, P. Li, H. Liu, L. Shi, J. Ye, Engineering the edges of MoS$_2$(WS$_2$) crystals for difect exfoliation into monolayers in polar micromolecular solvent, J. Am. Chem. Soc. 138 (2016) 14962–14969.

[35] P. Hu, M. Long, Cobalt-catalyzed sulfate radical-based advanced oxidation: a review on heterogeneous catalysts and applications, Appl. Catal. B Environ. 181 (2016) 103–117.

[36] L. Chen, M. Tang, C. Chen, M. Chen, K. Luo, J. Xu, D. Zhou, F. Wu, Efficient bacterial inactivation by transition metal catalyzed auto-oxidation of sulfite, Environ. Sci. Technol. 51 (2017) 12663–12671.

[37] A. Farhat, J. Keller, S. Tait, J. Radjenovic, Removal of persistent organic contaminants by electochemically activated sulfate, Environ. Sci. Technol. 49 (2015) 14326–14333.

[38] D. Zhou, L. Chen, J. Li, F. Wu, Transition metal catalyzed sulfite auto-oxidation systems for oxidative decontamination in waters: a state-of-the-art minireview, Chem. Eng. J. 346 (2018) 726–738.

[39] C.J.M. Van der Ham, M.T.M. Koper, D.G.H. Hetterscheid, Challenges in reduction of dinitrogen by proton and electron transfer, Chem. Soc. Rev. 43 (2014) 5183–5191.

[40] D.N. Wordofa, S.L. Walker, H. Liu, Sulfate radical-induced disinfection of pathogenic Escherichia coli O157:H7 via iron-activated persulfate, Environ. Sci. Technol. Lett. 4 (2017) 154–160.

[41] I. Michael-Kordatou, M. Iacovou, Z. Frontistis, E. Hapeshi, D.D. Dionysiou, D. Fatta-Kassions, Erythromycin oxidation and ERY-resistant Escherichia coli in activation in urban wastewater by sulfate radical-based oxidation process under UV-C irradiation, Water Res. 85 (2015) 346–358.

[42] W. Deng, H. Zhao, F. Pan, X. Feng, B. Jung, A. Abdel-Wahab, B. Batchelor, Y. Li, Visible-light-driven photocatalytic degradation of organic water pollutants promoted by sulfite addition, Environ. Sci. Technol. 51 (2017) 13372–13379.

[43] H. Lee, H. Kim, S. Weon, W. Choi, Y.S. Hwang, J. Seo, C. Lee, J.-H. Kim, Activation of persulfates by graphitized nanodiamonds for removal of organic compounds, Environ. Sci. Technol. 50 (2016) 10134–10142.

[44] J. Lim, D. Kwak, F. Sieland, C. Kim, D.W. Bahnemann, W. Choi, Visible light-induced catalytic activation of peroxymonosulfate using heterogeneous surface complexes of amino acids on TiO$_2$, Appl. Catal. B: Environ. 225 (2018) 406–414.

[45] Y. Jo, C. Kim, G. Moon, J. Lee, T. An, W. Choi, Activation of peroxymonosulfate on visible light irradiated TiO$_2$ via a charge transfer complex path, Chem. Eng. J. 346 (2018) 249–257.